VETERINARY QUARTERLY
2026, VOL. 46, NO. 1, 2672558
https://doi.org/10.1080/01652176.2026.2672558

Taylor & Francis
by informa

RESEARCH ARTICLE

OPEN ACCESS Check for updates

Magnetic nanohydroxyapatite–peptide silk fibroin hydrogel induces osteogenesis in canine periodontal ligament stem cells revealed by proteomic analysis

Steven Dwi Purbantoro[a,b,c], Marta Scatena[d], Teeanutree Taephatthanasagon[b,c], Watchareewan Rodprasert[b,c], Poorichaya Somparn[e], Saharat Nanthawong[e], Jiradej Makjaroen[e,f], Pongsakorn Jantaratana[g], Rangsini Mahanonda[h,i], Noppadol Sa-Ard-Iam[h,i], Thanaphum Osathanon[j,k,l], Sirinun Pisamai Tabtieang[m], Chenphop Sawangmake[b,c,l,n] and Sirirat Rattanapuchpong[b,c,o]

[a]The International Graduate Program of Veterinary Science and Technology (VST), Faculty of Veterinary Science, Chulalongkorn University, Bangkok, Thailand; [b]Veterinary Stem Cell and Bioengineering Innovation Center (VSCBIC), Faculty of Veterinary Science, Chulalongkorn University, Bangkok, Thailand; [c]Center of Excellence for Veterinary Clinical Stem Cells and Bioengineering, Faculty of Veterinary Science, Chulalongkorn University, Bangkok, Thailand; [d]Department of Bioengineering, University of Washington, Seattle, WA, USA; [e]Center of Excellence in Systems Biology, Faculty of Medicine, Chulalongkorn University, Bangkok, Thailand; [f]Department of Transfusion Medicine and Clinical Microbiology, Faculty of Allied Health Sciences, Chulalongkorn University, Bangkok, Thailand; [g]Department of Physics, Faculty of Science, Kasetsart University, Bangkok, Thailand; [h]Immunology Research Center, Faculty of Dentistry, Chulalongkorn University, Bangkok, Thailand; [i]Center of Excellence in Periodontal Disease and Dental Implant, Chulalongkorn University, Bangkok, Thailand; [j]Department of Anatomy, Faculty of Dentistry, Chulalongkorn University, Bangkok, Thailand; [k]Center of Excellence for Dental Stem Cell Biology, Faculty of Dentistry, Chulalongkorn University, Bangkok, Thailand; [l]Center of Excellence in Regenerative Dentistry (CERD), Faculty of Dentistry, Chulalongkorn University, Bangkok, Thailand; [m]Department of Surgery, Faculty of Veterinary Science, Chulalongkorn University, Bangkok, Thailand; [n]Department of Pharmacology, Faculty of Veterinary Science, Chulalongkorn University, Bangkok, Thailand; [o]Academic Affairs, Faculty of Veterinary Science, Chulalongkorn University, Bangkok, Thailand

ABSTRACT

The architecture of bone defects presents a challenge in designing scaffolds that support structural integrity and enhance osteoinduction. To address this, a noninvasive injectable silk fibroin (SF)-based hydrogel incorporating magnetic nanohydroxyapatite (MHAp) and osteogenic growth peptide (OGP) was developed. This study investigated the osteogenic differentiation potential of the hydrogel and its underlying mechanism on canine periodontal ligament stem cells (cPDLSCs). The incorporation of MHAp and/or OGP significantly enhanced osteogenic differentiation as evidenced by increased alkaline phosphatase activity, osteogenic marker expression, and biomineralization. Proteomics analysis revealed that TGF-β, BMP, and Notch signaling pathways were involved in hydrogel-induced osteogenic differentiation, which was further validated by an inhibition assay. Overall, the injectable SF hydrogel containing MHAp and OGP demonstrates strong potential for clinical application in the treatment of alveolar bone defects.

ARTICLE HISTORY
Received 24 November 2025
Accepted 4 May 2026

KEYWORDS
Alveolar bone defect; bone regeneration; canine periodontal ligament stem cells (cPDLSCs); injectable hydrogel; magnetic nanohydroxyapatite (MHAp); osteogenic growth peptide (OGP); silk fibroin (SF); proteomics

CONTACT Sirirat Rattanapuchpong sirirat.ra@chula.ac.th Academic Affairs, Faculty of Veterinary Science, Chulalongkorn University, Bangkok 10330, Thailand

Supplemental data for this article can be accessed online at https://doi.org/10.1080/01652176.2026.2672558.

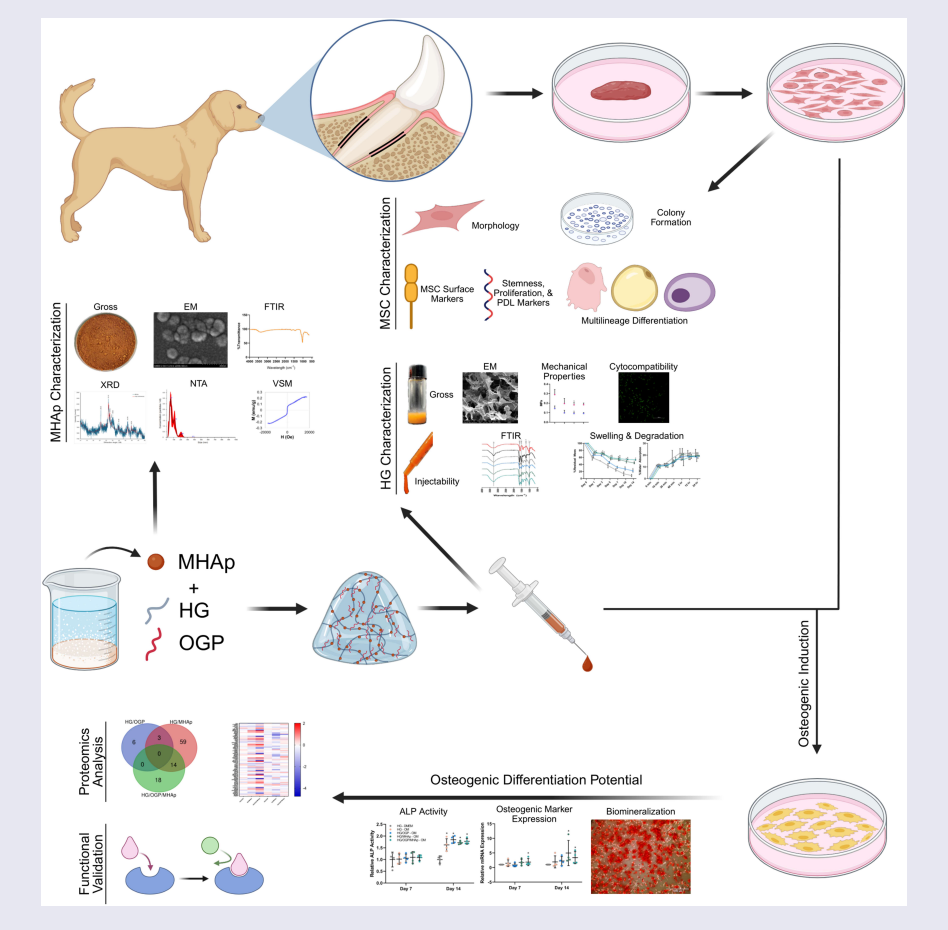

Introduction

Periodontitis is an inflammatory condition affecting the periodontal tissues, which occurs not only in human but also in animals, such as dog, cat, deer mouse, and *Macaca mulatta* (Wiebe et al. 2001; Niemiec 2008; Colombo et al. 2017). The condition is caused by bacterial infections, mainly *Porphyromonas gingivalis*, *Tannerella forsythia*, and *Treponema denticola*. The periodonthopathogenic bacteria resides on the tooth surface and progress to form biofilm on the gingival inducing inflammation, which induces the expression of matrix metalloproteases (MMPs) and apoptosis-related cytokines. This leads to the destruction of the gingival tissue and results in the formation of a periodontal pocket. The progression also destroys the periodontal ligament by the increased expression of MMPs, leading to the attachment loss (Könönen et al. 2019). In severe periodontitis, the microstructure of cementum is altered, assumed the periodontopathogenic bacteria affects acid/base and oxidation/reduction reactions against the organic matrix, altering the surface integrity andcytokine to breakdown ECM (Junka et al. 2015; Li et al. 2019). It leads to bone defects in the alveolar bone due to the progression of bone resorption (Niemiec 2008). The progression starts when periopathogens produce harmful products and enzymes that disintegrate the extracellular matrix in the bone tissue. Moreover, when lipopolysaccharides of periopathogens and infiltrated leukocyte-derived interleukin 1 are exposed to osteoblasts and periodontal ligament fibroblasts, RANKL is expressed, increasing the RANKL/OPG ratio to promote osteoclast development leading to bone resorption (Hienz et al. 2015). The bone resorption subsequently causes bone loss, which can be horizontal, vertical, and/or furcation defects, which can be visualized by radiographs (Kurt-Bayrakdar et al. 2024). If left untreated, advanced periodontitis-induced bone resorption can result in pathological fracture, which small-breed dogs are prone to this complication due to dental crowding (Gioso et al. 2001; Niemiec 2008; Scherer et al. 2019), causing significant burdens on both animals and their owners.

To prevent such complications, bone tissue engineering (BTE) has emerged as a promising strategy for bone regeneration. Guided bone regeneration (GBR) is a widely used technique in periodontal therapy for the treatment of bone defects. It involves the placement of a barrier membrane over the defect to promote selective cell repopulation. The membrane prevents the rapid migration of epithelial cells and fibroblasts into the defect site, thereby allowing slower-growing osteogenic cells to populate the area and facilitate new bone formation. Additionally, the membrane helps maintain a stable space for blood clot formation, which serves as a scaffold for tissue regeneration and prevents soft tissue collapse into the defect (Hitti and Kerns 2011). However, the irregular architecture of either horizontal, vertical, or furcation bone defects remains a major challenge to overcome. A minimally invasive approach using an injectable polymer derived from *Bombyx mori*, has attracted attention due to its biocompatibility, injectability, and capacity to support bone regeneration (Ciocci et al. 2018; Wang et al. 2020; Chuysinuan et al. 2021; Sun et al. 2021). Notably, SF lysates have also demonstrated potential in reducing osteoclastogenesis and promoting osteoclast apoptosis (Jones et al. 2009; Chon et al. 2012).

The functionality of SF-based hydrogel can be enhanced by incorporating additional bioactive components. Magnetic nanohydroxyapatite (MHAp), a modified form of nanohydroxyapatite with intrinsic bone-like composition, has shown superior regenerative properties compared to its nonmagnetic counterpart (Hu et al. 2018; Russo et al. 2018). Previous studies have demonstrated that the integration of magnetic particles into SF hydrogel improves their osteoinductive potential (Tanasa et al. 2020; Ma et al. 2022). Furthermore, osteogenic growth peptide (OGP), a 14-amino acid peptide, has been shown to enhance the osteogenic differentiation of mesenchymal stem cells (MSCs) (Vanella et al. 2010; Chen et al. 2011; Purbantoro et al. 2022).

Based on this knowledge, the present study aimed to develop an injectable silk fibroin hydrogel incorporating MHAp and OGP and to evaluate its potential and underlying mechanisms. Canine periodontal ligament stem cells (cPDLSCs) were used as a model due to their known osteogenic potential and their origin within the alveolar bone socket (Zhu and Liang 2015). Proteomics analysis was employed to further elucidate the signaling pathways involved in hydrogel-induced osteogenic differentiation of cPDLSCs.

Materials and methods

Canine periodontal ligament stem cell (cPDLSC) isolation and culture

The study protocol to use cPDLSCs has been approved by the Institutional Animal Care and Use Committee (IACUC), Faculty of Veterinary Science, Chulalongkorn University (Animal Use Protocol No. 2231041). The mid-third portion of periodontal ligament tissues from clinically healthy donor dogs post-jaw trauma and/or with malocclusion requiring tooth extraction without periodontal disease signs, according to the American Veterinary Dental College (AVDC), was harvested from the Small Animal Teaching Hospital, Faculty of Veterinary Science, Chulalongkorn University, upon the owner's consent for the study participation. The collected tissue was explanted and cultured in growth medium that contains Dulbecco's Modified Eagle Medium (DMEM) (Cat#12800-017) supplemented with 10% fetal bovine serum (FBS) (Cat#10270-106), 1% GlutaMAX™-I (Cat#35050-061), 1% antibiotic-antimycotic (Cat#15240-062). Cells were subcultured at 70%–80% confluency. Cells at passages 3–5 were used in this study.

Flow cytometry

Flow cytometry was performed to analyze the MSC markers (CD73, CD90, CD44, and CD29) and hematopoietic stem cell (HSC) marker (CD45). Single cPDLSC suspension was stained with FITC-conjugated mouse anti-human CD45 monoclonal antibody (mAb) (Cat#368508), FITC-conjugated mouse anti-human CD73 mAb (Cat#344016), FITC-conjugated goat anti-mouse IgG secondary antibody (Cat#STAR117F), PE-conjugated rat anti-dog CD90 mAb (Cat#1TFS-AB-12-5900-42), Alexa Fluor 488-conjugated rat anti-dog CD44 mAb (Cat#MCA1041A488), and PE-conjugated mouse anti-human CD29 mAb (Cat#3303004). FITC-conjugated mouse IgG1 kappa Isotype (Cat#400110), mouse IgG2a kappa Isotype (Cat#400201), and PE-conjugated rat IgG2b kappa Isotype (Cat#400608) were employed in this study as isotype controls. The stained cells were analyzed using a FACSCalibur flow cytometer.

Reverse transcription quantitative polymerase chain reaction (RT-qPCR)

Total mRNA was extracted using the Zymo kit (Cat# R2052) following the manufacturer's protocol from previously collected cells in TRIzol™ (Cat#15596026). Conversion of mRNA into cDNA was done with a Promega kit (Cat#A3800). Next, RT-qPCR was performed using LUNA Master Mix (Cat#M3003L) on a CFX Connect™ Optics Module (BioRad), and the cycle threshold was measured with Bio-Rad CFX Maestro software. The calculation of mRNA expression used the following formula of $2^{-\Delta Ct}$, whereas $\Delta Ct = Ct_{target\ gene} - Ct_{reference\ gene}$. As for experiments with more than one group, the expression was calculated by comparing with the control group with the following formula of $2^{-\Delta\Delta Ct}$, whereas $\Delta\Delta Ct = \Delta Ct_{treatment\ group} - \Delta Ct_{control\ group}$. The calculation was normalized to *GAPDH* as the reference gene. Primer sequences used in this study are shown in Supplementary Table S1.

Colony-forming assay

A 1.5×10^3 cells in a 60-mm dish, cPDLSCs were seeded and maintained for 14 days in growth medium. Cells were then fixed with cold methanol at 4 °C for 20 min and stained with crystal violet (Cat#94448). The stained cells were subjected to a colony count with the criterion that one colony contains at least 50 cells.

Osteogenic differentiation in vitro

Following the previous study (Nantavisai et al. 2020), cPDLSCs were seeded at 3.5×10^4 cells/well in a 24-well plate and cultured for 14 days. The cells were induced under osteogenic medium that was growth medium supplemented with 50 µg/mL ascorbic acid (Cat#A4034), 250 nM dexamethasone (Cat#D4902), and 5 mM β-glycerophosphate (Cat#G9422).

Alizarin Red S staining

Prior to staining, the osteogenic-induced cells were fixed with cold methanol at 4 °C for 20 min. The fixed cells were then stained with 2% Alizarin Red S solution (Cat#A5533) in distilled water at pH 4.2 at RT.

Adipogenic differentiation in vitro

At a density of 3×10^4 cells, cPDLSCs were seeded in a 24-well plate and maintained for 23 days to be differentiated into adipogenic lineage following previous studies (Nantavisai et al. 2020; Rodprasert et al. 2021; Dang Le et al. 2022; Purbantoro et al. 2022; Purwaningrum et al. 2023) With four induction cycles, adipogenic induction medium contains growth medium supplemented with 1 µM dexamethasone, 0.1 mM indomethacin (Cat#I7378), 1 mM 3-isobutyl-1-methylxanthine (IBMX) (Cat#I5879), and 1 µg/mL insulin (Cat#I6634) was used for 72 h and adipogenic maintain medium contains growth medium supplemented with 1 µg/mL insulin was used for the next 24 h.

Oil Red O staining

A 4% formaldehyde solution was used to fix the adipogenic-induced cPDLSCs for 1 h. The cells were then stained with 0.1% Oil Red O solution (Cat#O0625) in isopropanol and kept in PBS for observation.

Chondrogenic differentiation in vitro

The chondrogenic differentiation was performed according to previous studies (Nantavisai et al. 2020; Rodprasert et al. 2021; Dang Le et al. 2022; Purbantoro et al. 2022; Purwaningrum et al. 2023). The cPDLSCs were seeded at 5×10^4 cells/well in a 24-well plate and maintained for 21 days under induction media consisting of growth medium supplemented with 15% FBS, 10 ng/mL transforming growth factor (TGF)-β3, 50 µg/mL ascorbic acid, 0.4 mg/mL L-Proline (Cat#P0380), 0.1 µM dexamethasone, and 1% insulin-transferrin-selenium (Sueishi et al. 2020) (Cat#41400045).

Alcian blue staining

A 0.1% alcian blue (Cat#A5268) solution in 3% acetic acid was used to fix the cells after cell fixation with 4% paraformaldehyde for 1 h.

Magnetic nanohydroxyapatite synthesis and characterization

The synthesis of MHAp followed the study of Wu et al. (2007). In brief, 0.3 M orthophosphoric acid (H_3PO_4, Cat#695017) was added at 3 mL/min rate into a 0.5 M calcium hydroxide ($Ca(OH)_2$, CAS#1305650) at 85 °C in a shaking water bath with 100 rpm to create a stoichiometric amount at 1.67 Ca/P molar ratio. Ammonium hydroxide solution (NH_4OH, Cat#221228) was then added to the mixture to adjust the pH to 8.5. The mixture was stirred for 2 h at 400 rpm and allowed to age overnight at room temperature (RT). The next day, at a molar ratio $X_{Fe/Ca} = 0.8$, iron (II) chloride tetrahydrate ($FeCl_2{\cdot}4H_2O$, Cat#44939) was added into the aged suspension with a rate of 1 mL/min at 85 °C in a shaking water bath at 100 rpm. The NH_4OH was added again to adjust the pH to 8.5. Another stirring for 2 h at 400 rpm and aging overnight at RT were done. The final aged suspension was termed as MHAp suspension and later washed with double-distilled water three times by stirring at 400 rpm for 1 min at RT and allowed to age for 2 h. The supernatant was discarded, and the aqueous suspension was freeze-dried for further use.

X-ray diffraction (XRD)

The MHAp crystal structure was analyzed with XRD (D8 Discover, Bruker) within a 2θ range of 10°–60° by Cuκα ($\lambda = 1.5406$ Å) radiation. The crystallite size and spectra were analyzed in reference to the hydroxyapatite (The International Center for Diffraction Data (ICDD) No. 01-074-0565) with Profex5 software.

Electron microscopy (EM) and energy dispersive X-ray spectroscopy (EDX)

The MHAp properties of morphology and element components were analyzed with a field emission scanning EM (FE-SEM) and EDX (S-4800). The hydrogels were analyzed for their morphology with an SEM (Quanta250). Both MHAp and hydrogels were coated on a carbon film on the surface by sputtering platinum (E-1010 Ion Sputter) and captured using 10 kV and 20 kV, respectively.

Nanotracking analysis (NTA)

The particle size distribution of MHAp was determined with an NTA (NanoSight NS300). The MHAp suspension in double-distilled water was injected by an automatic syringe pump. The results were analyzed with NanoSight NTA 3.2 software.

Fourier-transform infrared spectroscopy (FTIR)

An FTIR (Nicolet Nexus IS5) was used to analyze the functional groups of MHAp and hydrogels. Measurement of each spectrum was done for 32 scans between 650 and 4000 cm^{-1} wavelengths in the transmission mode by the potassium bromide (KBr) method. The results were shown in Percent Transmittance.

Vibrating sample magnetometer (VSM)

The MHAp magnetic property was analyzed with a VSM (custom-made by the Department of Physics, Kasetsart University, Thailand). An applied magnetic field at 15 kOe was used at RT. A 3 mm diameter Ni sphere (Lake Short 730908) was employed to calibrate the system as a standard reference. The result was shown as magnetization (*M*) for magnetic moment *m* per total mass of the specimen.

Hydrogel preparation

Preparation of hydrogel employed 5% silk fibroin (SF) solution (Cat#5154), 3% sodium alginate (SA) (Cat#W201502), and 100 mM calcium chloride ($CaCl_2$, CAS#10035048) in an aseptic condition, which each material had been autoclaved before, to reach final concentration at 2%, 1.3%, and 16.67% v/v, respectively, by ultrasonication (CE-1100D) at RT. Before the addition of $CaCl_2$, OGP (Cat#HYP1563) and/or MHAp were added into the mixture and ultrasonicated at RT. The final product was used freshly for the cell culture, while freeze-dried for characterization. Extract media was collected by incubating fresh hydrogel in respective media at a ratio of 0.2 g/mL, according to the ISO 10993-12-2021.

Injectability assay

The injectability property of the hydrogels was determined by the injectability assay. A 500 µL of each hydrogel was loaded in a 1 mL syringe without or with a needle (18 G, 21 G, 22 G, or 23 G). The loaded syringe was placed vertically to bear 200 g for 10 s. The Percent Injectability was calculated by the following equation:

$$\%\text{Injectability} = \frac{\text{Preinjected mass(g)} - \text{Postinjected mass(g)}}{\text{Preinjected mass(g)}} \times 100\%.$$

Swelling assay

The capability of hydrogels to absorb water was evaluated using freeze-dried hydrogels for its water content by following the previous reported study (Torsahakul et al. 2022). The initial weight was measured as W_0. The hydrogels were then soaked in phosphate buffer saline (PBS, pH 7.4) in the incubator at 37 °C for 24 h. After incubation, tissue paper was used to blot the excess water for further weight measurement (W_t). The percent water absorption was calculated by the following equation:

$$\%\text{Water Absorption} = \frac{W_t - W_0}{W_t} \times 100\%.$$

In vitro enzymatic degradation

Following the previous study (Torsahakul et al. 2022), the assay employed the degradation solution containing 1 U/mL protease XIV (pH 7.4, Cat#P5147) and 0.01% w/v sodium azide (Cat#S2002) in PBS (pH 7.4). Before immersion in the solution, the freeze-dried hydrogels were weighed (W_0) and later incubated at 37 °C for 14 days with an interval of 2 days for solution replacement. After incubation, the immersed hydrogels were washed with distilled water and centrifuged at 10,000 rpm for 5 min and dried in an oven at 60 °C overnight. The dried hydrogels were weighed (W_t) and calculated for percent degradation with the following equation:

$$\%\text{Degradation} = \frac{W_0 - W_t}{W_0} \times 100\%.$$

Mechanical property

Freeze-dried hydrogels were analyzed in a Universal Testing Machine (EZ-S 500 N, SHIMADZU) to determine mechanical properties with a load of 500 N, with a constant strain rate at 1 mm/min.

Resazurin assay

Proliferation of cells was analyzed using resazurin (Cat#R7017) solution in growth medium at a final concentration of 0.015 mg/mL. The cells were incubated for 3 h before absorbance measurement at 570 and 600 nm wavelengths with a spectrophotometer.

Live/dead assay

Live/dead assay was performed by following the previous study (Purbantoro et al. 2022). The assay employed Calcein-AM (Cat#C1430) and propidium iodide (PI) (Cat#P21493) in PBS by incubating the cells for 20 min. The stained cells were observed under a confocal microscope.

Alkaline phosphatase (ALP) activity assay

Before the start of the reaction, cells were lysed using a lysis buffer consisting of 0.1% Triton X-100, 1 M Tris–HCl, and 5 mM $MgCl_2$ according to previous reports (Sawangmake et al. 2016; Nantavisai et al. 2020; Purbantoro et al. 2022; Purwaningrum et al. 2023). The lysate was incubated with p-nitrophenol phosphate (PNPP) (Cat#002201), 2-amino-2-methyl-1-propanol (Cat#A65182), and 2 mM MgCl2 for 15 min at 37 °C. A 0.1 M NaOH solution was added to quench the reaction, and absorbance was measured using a spectrophotometer at 410 nm. Additionally, total protein concentration was measured with Qubit™ Protein Assay kit (Cat#Q33211) following the manufacturer's protocol. The ALP activity was calculated in the U/mg protein unit.

Protein extraction and in-solution digestion

Protein extraction was performed by following the protocol of the EasyPep™ Mini MS Sample Prep Kit (Cat#A40006), followed by protein concentration measurement using a bicinchoninic acid (BCA) assay kit (Cat#23225). Briefly, the protein in 1× protease inhibitor (Cat#87786) and 8 M urea in 100 mM tetraethylammonium bromide (TEAB) was reduced and alkylated using tris(2-carboxyethyl) phosphine (TCEP) and iodoacetamide (IA), respectively. The samples were then digested and quenched after incubation for 3 h. The peptides were then cleaned up with the same sample preparation kit and evaporated using vacuum centrifugation. The products were then resuspended in 0.1% formic acid (FA). The digested proteins were quantified using a Pierce™ Quantitative Fluorescent Peptide Assay (Cat#23290).

LC–MS/MS and analysis

The resuspended samples were injected into the EASY nLC1000 system (Thermo Scientific) connected to a Q-Exactive Orbitrap Plus mass spectrometer (Thermo Scientific) supplied with a nano-electrospray ion source (Thermo Scientific) at a flow rate of 300 nL/min. Target peaks were selected at a range of 350–1400 m/z from the MS scan. Data acquisition and identification were performed using FragPipe v21.1 software using default settings for the label-free quantification (LFQ) method.

Proteomics quantification

The identified proteins were annotated using FragPipe-Analyst (http://fragpipe-analyst.nesvilab.org/) to exclude the proteins found in less than three replicates. The Log2 value was calculated as a result of the normalized ratio for mean and standard deviation of fold change and tested with an independent *t*-test to compare between groups. Proteomics analysis and visualization were made using https://bioinformatics.psb.ugent.be/webtools/Venn/, Instant Clue v0.12.2, String (https://string-db.org/), SRplot (Tang et al. 2023), and Reactome (https://reactome.org/).

Inhibition assay

Validation was performed under osteogenic induction conditions by the addition of an inhibitor of each relevant selected pathway for the biomineralization. The inhibitors used in this study included 4 µM Dorsomorphin (Cat#P5499), 100 ng/mL Dickkopf 1 (Dkk-1) (Cat#SRP3258), 4 µM SB-431542 (Cat#S4317), and 25 µM DAPT (Cat#D5942) for BMP, canonical Wnt, TGF-β, and Notch signaling pathways, respectively.

Statistical analysis

Comparison of more than two groups was done by using the Kruskal–Wallis test and followed by the Mann–Whitney U test for two independent groups with SPSS Statistics. *p* value less than 0.05 was used in this study as a significant level.

Results

MHAp was successfully synthesized with nanoscale and superparamagnetic properties

MHAp was successfully synthesized by the coprecipitation method as brown-colored powder (Figure 1A). X-ray diffraction (XRD) analysis revealed that the crystal structure of MHAp closely resembled that of reference hydroxyapatite, with a calculated crystallite size of 42.4 nm (Figure 1B). Field-emission scanning electron microscopy (FE-SEM) presented spherical nanoparticles with an average diameter of approximately 87 nm (Figure 1C). Consistent with XRD and FE-SEM findings, nanoparticle tracking analysis (NTA) indicated a mode particle size of 56.4 nm (Figure 1D). Fourier-transform infrared spectroscopy (FTIR) identified characteristic absorption peaks at 659, 860, 1029, and 3375 cm^{-1}, confirming the presence of phosphate and hydroxyl functional groups typical of hydroxyapatite (Figure 1E). In addition, magnetic property analysis demonstrated that the synthesized MHAp exhibited superparamagnetic behavior (Figure 1F), confirming its suitability for biomedical applications requiring magnetic responsiveness.

OGP and MHAp exhibit proliferative effects without inducing cytotoxicity in cPDLSCs

Before experimentation, the isolated cPDLSCs were characterized and confirmed to exhibit MSC properties. The cells displayed spindle-shaped morphology, expressed stemness and periodontal ligament markers, demonstrated colony-forming ability, and differentiated into multiple lineages (Figure 2).

Cytocompatibility was assessed by treating the cells with OGP at concentrations ranging from 0.01 to 1000 nM and MHAp at 0.2%–1% (%w/v) for up to 7 days in growth medium. Cell proliferation was evaluated using the resazurin assay, and cell viability was confirmed by live/dead (L/D) staining (Figure 3A).

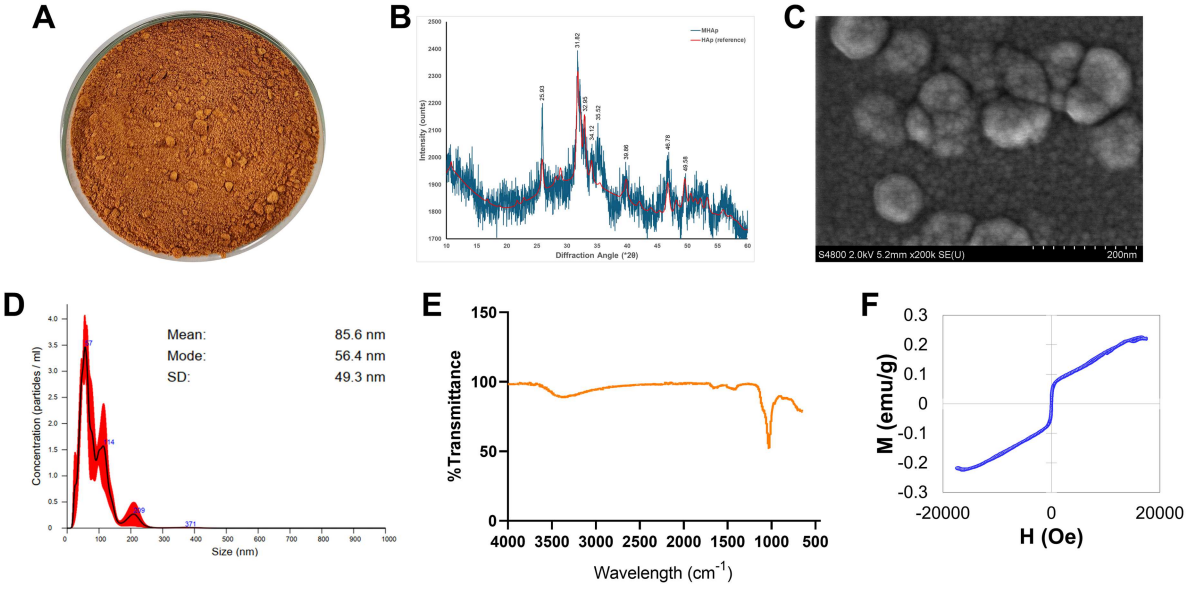

Figure 1. Characterization of synthesized MHAp. (A) Gross appearance of MHAp. (B) XRD analysis of MHAp compared to the reference HAp (ICDD No. 01-074-0565). (C) Morphology of MHAp by FE-SEM analysis at 200,000× magnification. (D) NTA analysis of MHAp ($n = 3$, representative image from three replicates). (E) FTIR analysis of MHAp. (F) Magnetic property of MHAp by VSM analysis.

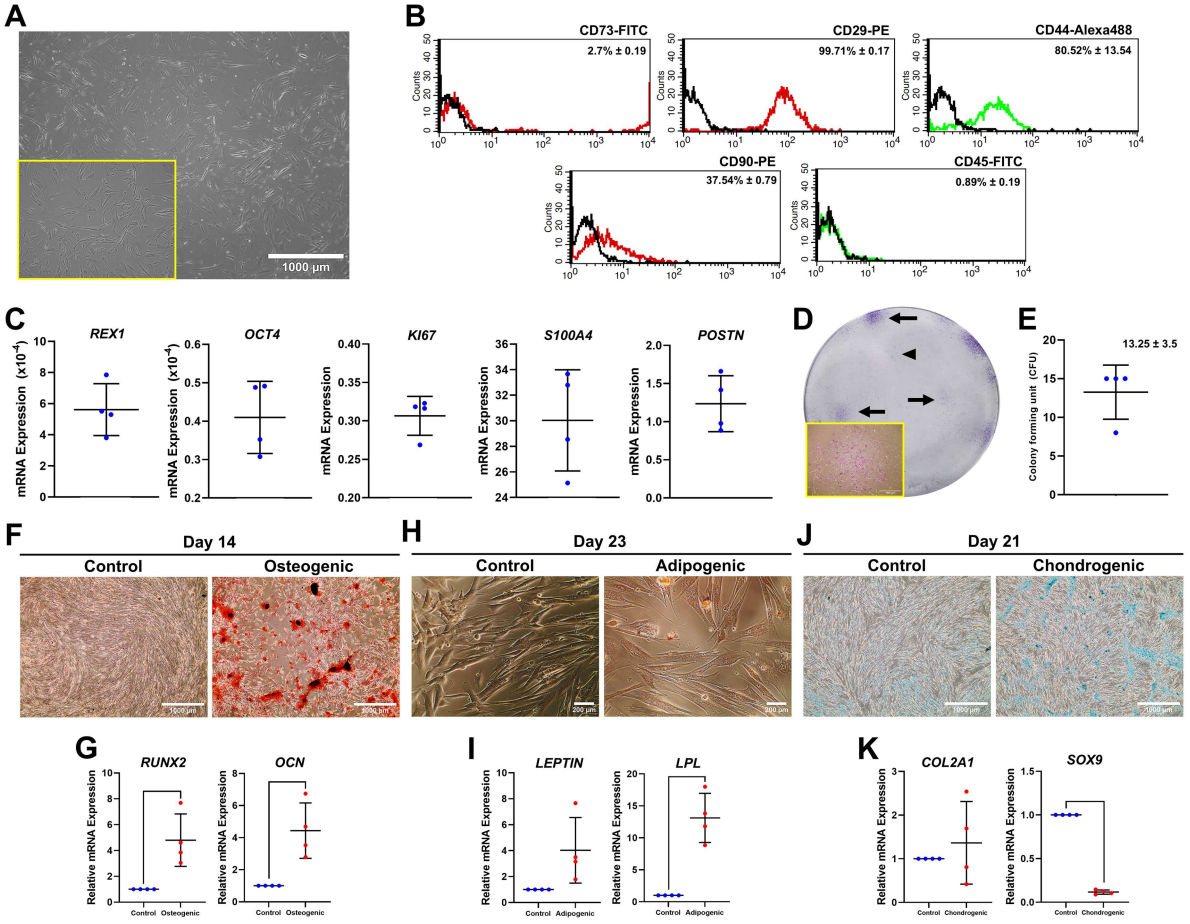

Figure 2. Characterization of cPDLSCs. (A) Morphology of isolated cPDLSCs (phase contrast microscopy representative image). (B) Surface marker expression of cPDLSCs by flow cytometry analysis ($n = 4$). (C) Expression of stemness, proliferation, and PDL markers by RT-qPCR normalized with *GAPDH* as the reference gene ($n = 4$). (D) Colony formation of cPDLSCs ($n = 4$, representative image from four replicates). (E) Quantification of cPDLSC colony formation ($n = 4$). (F) Biomineralization staining of osteogenic lineage differentiation of cPDLSCs by Alizarin Red S staining (representative image from four replicates). (G) Osteogenic marker expression of osteogenic lineage differentiation of cPDLSCs by RT-qPCR normalized with *GAPDH* as the reference gene ($n = 4$). (H) Extracellular matrix staining of chondrogenic differentiation of cPDLSCs by alcian blue staining (representative image from four replicates). (I) Chondrogenic marker expression of chondrogenic differentiation of cPDLSCs by RT-qPCR normalized with *GAPDH* as the reference gene ($n = 4$). (J) Lipid droplet staining of adipogenic differentiation of cPDLSCs by Oil Red O staining (representative image from four replicates). (K) Adipogenic marker expression of adipogenic lineage differentiation of cPDLSCs by RT-qPCR normalized with *GAPDH* as the reference gene ($n = 4$). Arrow indicates a colony, and arrowhead indicates a noncolony. Bar indicates $p < 0.05$, Mann–Whitney test; line indicates mean and standard deviation.

The OGP treatment significantly enhanced cell proliferation starting from day 1 at 0.1, 1, 10, and 100 nM, with sustained effects through days 5 and 7. Notably, only the 100 nM concentration exhibited a statistically significant difference compared to the control (Figure 3B). The L/D staining showed minimal red-stained (dead) cells, confirming the absence of cytotoxicity (Figure 3D).

The MHap did not initially promote proliferation compared to the control. However, by day 5, a dose-dependent increase in proliferation was observed relative to day 5 control group, despite an overall decrease compared to day 1 (Figure 3C). On day 7, lower concentrations of MHAp (0.2, 0.4, and 0.6% w/v) supported greater proliferation than higher concentrations (0.8 and 1% w/v). Similar to OGP, MHAp treatment resulted in negligible cytotoxicity, as evidenced by the absence of red-stained dead cells in L/D staining (Figure 3E). These results indicate that both OGP and MHAp promote proliferation and are cytocompatible with cPDLSCs *in vitro*.

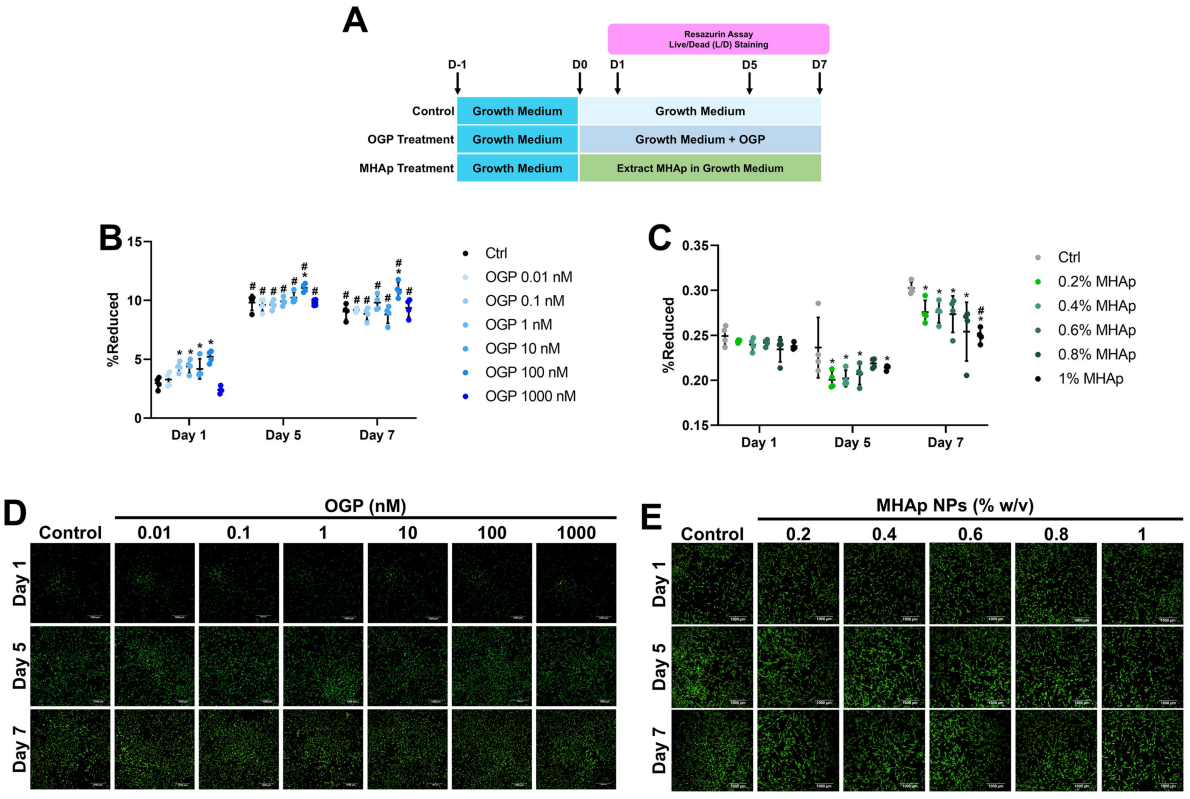

Figure 3. Cytocompatibility of OGP and MHAp on cPDLSCs. (A) Experimental design. The OGP at 0.1 to 1000 nM and MHAp at 0.2% to 1% w/v were used as treatment on cPDLSCs for resazurin assay and live/dead (L/D) staining for 7 days of culture. (B) Proliferation effect of OGP on cPDLSCs by resazurin assay ($n = 4$). (C) Proliferation effect of MHAp on cPDLSCs by resazurin assay ($n = 4$). (D) Viability of cPDLSCs under OGP treatment by L/D staining ($n = 4$, representative image from four replicates). Green indicates viable cells and red indicates dead cells. (E) Viability of cPDLSCs under MHAp treatment by L/D staining ($n = 4$, representative image from four replicates). Green indicates viable cells and red indicates dead cells. * and # indicate the statistically significant difference to the control each day and to the respective group on day 1, respectively, at $p < 0.05$, Mann–Whitney test; line indicates mean and standard deviation.

Hydrogel characteristics

Based on previous experiments, concentrations at 100 nM for OGP and 0.6% w/v for MHAp were selected for subsequent studies. The gross morphology of hydrogels before and after crosslinking is shown in Figure 4A. There was no difference between HG and HG/OGP with a clear appearance, while HG/MHAp and HG/OGP/MHAAp showed a brownish and opaque appearance.

Injectability assay revealed that all hydrogels were easily extruded using 18 G, 21 G, and 22 G needles, with up to ~98% injectability. However, the use of a 23 G needle significantly reduced injectability up to ~70% (Figure 4B). Scanning electron microscopy (SEM) revealed an interconnected porous structure in all hydrogels, with average and standard deviation of pore size distribution at 61.18 ± 20.94, 54.66 ± 18.07, 54.88 ± 14.20, and 47.23 ± 14.09 µm for HG, HG/OGP, HG/MHAp, and HG/OGP/MHAp, respectively (Figure 4C,D). The FTIR spectroscopy showed characteristic peaks around 3265, 1636, 1534, 1239, and 1028 cm^{-1}, confirming the chemical composition of the silk-fibroin-based hydrogel and its modifications (Figure 4E).

In degradation studies, HG/OGP/MHAp showed the lowest degradation rate over 14 days, followed by HG/MHAp, HG/OGP, and HG alone. Conversely, the swelling assay indicated that unmodified HG appeared to have the highest swelling ratio, followed by OGP- and/or MHAp-incorporated hydrogels. Most groups reached equilibrium within 2 h (Figure 4F). Mechanical testing revealed that incorporation of OGP and/or MHAp reduced both Young's modulus and compressive strength compared to unmodified HG (Figure 4G). Cytocompatibility testing, as schemed in Figure 4H, demonstrated enhanced cell proliferation in all hydrogel groups containing OGP and/or MHAp compared to the HG group and untreated control (Figure 4I). Additionally, L/D staining

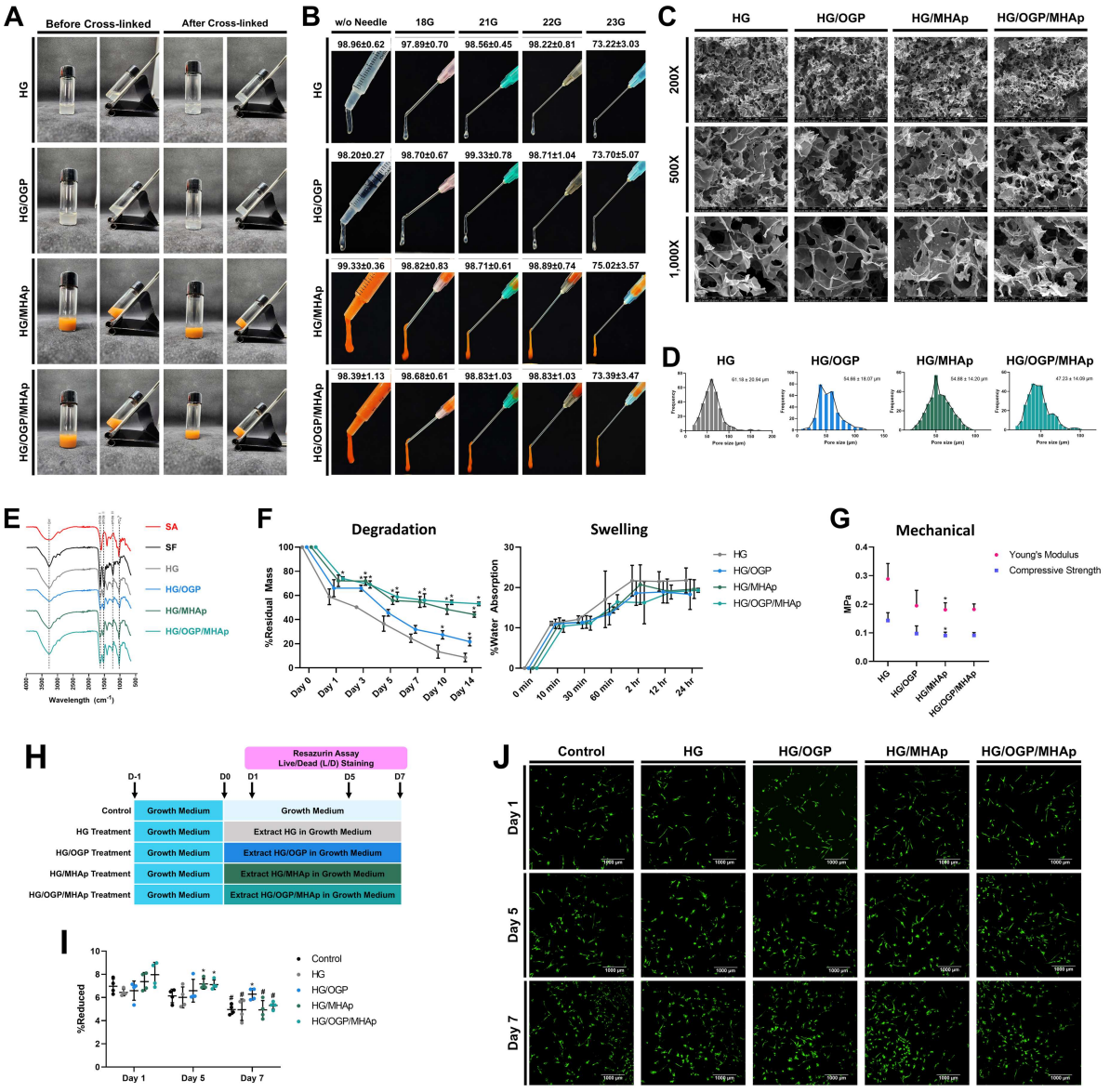

Figure 4. Characteristics of hydrogels. (A) Gross appearance of hydrogels before and after cross-linking with $CaCl_2$. (B) Injectability and quantification of hydrogels without and with needles of 18, 21, 22, and 23 G ($n = 4$, representative image from four replicates). (C) Morphology of freeze-dried hydrogels at 200, 500, and 1000× by SEM analysis (representative image). (D) Pore distribution quantification of (C) from 300 pores. (E) FTIR analysis of sodium alginate (SA), silk fibroin (SF), and hydrogels. (F) Degradation and swelling profiles of hydrogels. (G) Mechanical properties of hydrogels. (H) Experimental design. Extract hydrogels were used to treat cPDLSCs for the resazurin assay and L/D staining for 7 days of culture. (I) Proliferation effect of hydrogels on cPDLSCs by resazurin assay ($n = 4$). (J) Viability of cPDLSCs under hydrogel treatment by L/D staining ($n = 4$, representative image from four replicates). Green indicates viable cells and red indicates dead cells. * and # indicate the statistically significant difference to the control each day and to the respective group on day 1, respectively, at $p < 0.05$, Mann–Whitney test; line indicates mean and standard deviation.

confirmed the absence of cytotoxicity, with no observable, red-stained dead cells in any group (Figure 4J). Overall, the incorporation of OGP and MHAp improved several functional properties of the SF hydrogel, including bioactivity, injectability, degradation behavior, and cytocompatibility.

HG/OGP/MHAp possessed osteogenic differential potential of cPDLSCs in vitro

To assess the osteogenic differentiation potential, monolayer cPDLSCs were treated with OM and extraction media from the hydrogels and evaluated for alkaline phosphatase (ALP) activity, osteogenic gene

expression, and biomineralization, as outlined in the experimental scheme in Figure 5A. The ALP activity was enhanced in all groups treated with OGP and/or MHAp-incorporated hydrogels on both days 7 and 14, with the highest activity observed in the HG/OGP/MHAp group (Figure 5B). Quantitative PCR analysis revealed the upregulation of osteogenic-related genes *Runx2*, *OSX*, and *Col1A1* on day 7 in OGP- and/or MHAp-treated groups. On day 14, *Runx2* and *ALP* were upregulated, while *OSX* and *Col1A1* expression levels decreased (Figure 5C), suggesting temporal regulation of osteogenic markers during differentiation. Alizarin Red S staining confirmed enhanced biomineralization in cells treated with hydrogels containing OGP and/or MHAp, with the most pronounced in the HG/OGP/MHAp group (Figure 5D,E). These findings indicate that the injectable silk fibroin hydrogel containing both OGP and MHAp effectively promotes osteogenic differentiation of cPDLSCs *in vitro*.

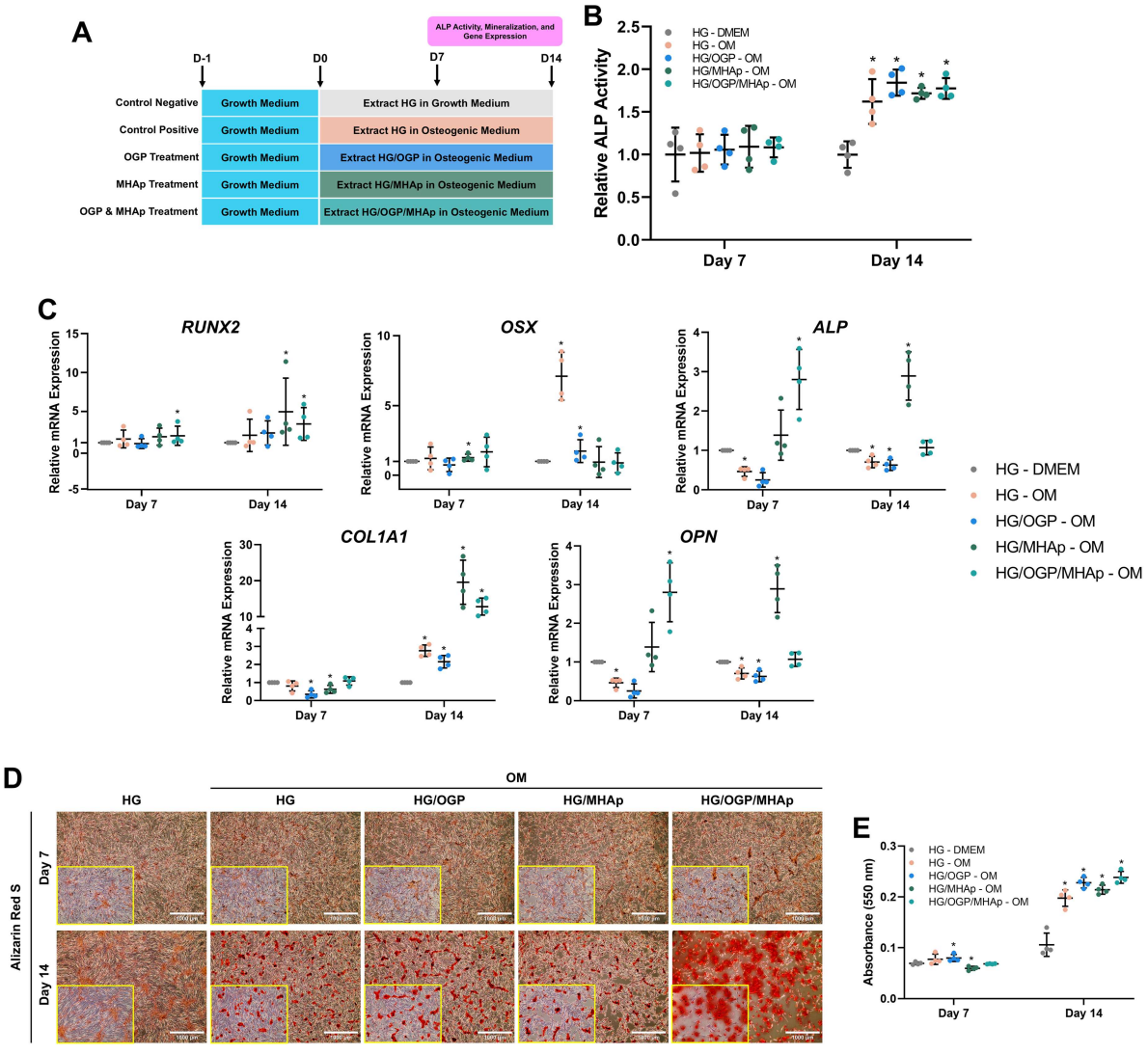

Figure 5. Osteogenic differentiation potential of cPDLSCs under hydrogel treatment. (A) Experimental design. Extract hydrogels were used to treat cPDLSCs under osteogenic induction medium for alkaline phosphatase (ALP) activity, osteogenic marker expression, and biomineralization staining for 14 days of culture. (B) The ALP activity of cPDLSCs under hydrogel treatment by ALP assay ($n = 4$). (C) Osteogenic marker expression of cPDLSCs under hydrogel treatment by RT-qPCR normalized with *GAPDH* as the reference gene ($n = 4$). (D) Biomineralization staining of cPDLSCs under hydrogel treatment by Alizarin Red S staining (representative image from four replicates). (E) Quantification of (D) by the elution method ($n = 4$). * indicates the statistically significant difference to the control each day at $p < 0.05$, Mann–Whitney test; line indicates mean and standard deviation.

Distinct proteome profiles induced by OGP and/or MHAp incorporation into hydrogel

To disseminate the mechanisms underlying hydrogel-induced osteogenic differentiation, proteomics profiling was conducted on cPDLSCs treated with hydrogels on days 7 and 14 (Figure 6A). On day 7, a total of eight proteins were commonly expressed across all hydrogel groups, while 9, 20, and 47 unique proteins were identified in HG/OGP, HG/MHAp, and HG/OGP/MHAp groups, respectively. In contrast, the day 14 analysis revealed no commonly shared proteins, with 6, 59, and 47 unique proteins identified in HG/OGP,

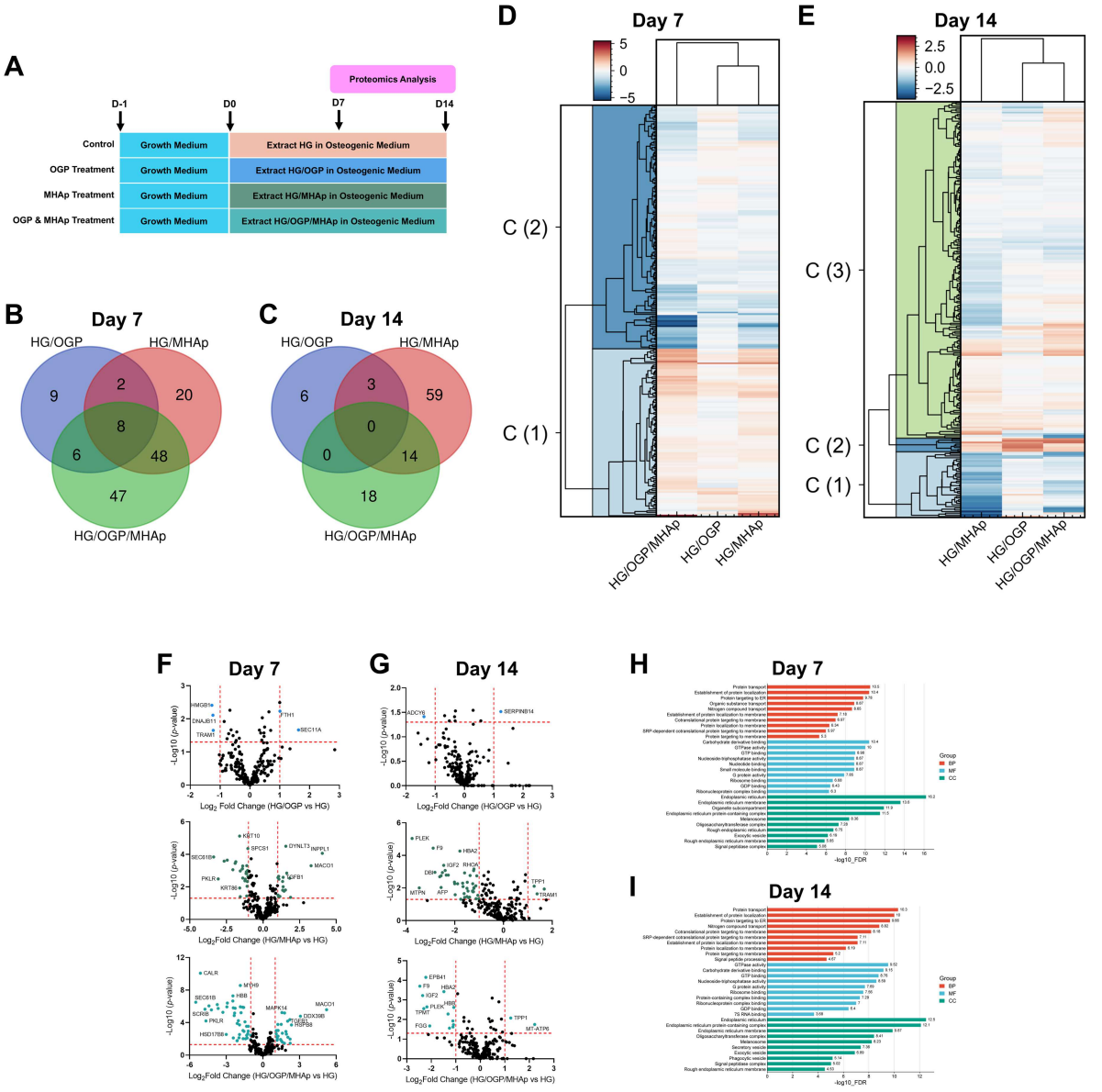

Figure 6. Proteomics analysis of cPDLSCs under hydrogel treatment toward osteogenic lineage. (A) Experimental design. Extract hydrogels were used to treat cPDLSCs under osteogenic induction medium for proteomics analysis for 14 days of culture ($n = 5$). (B) Venn diagram analysis of significantly expressed proteins from day 7, compared to HG as control. (C) Venn diagram analysis of significantly expressed proteins from day 14, compared to HG as control. (D) Cluster heat map analysis of identified proteins from day 7, compared to HG as control. (E) Cluster heat map analysis of identified proteins from day 14, compared to HG as control. (F) Volcano plot analysis of identified proteins from day 7, compared to HG as control. Blue dot indicates protein was significantly different at $p < 0.05$. (G) Volcano plot analysis of identified proteins from day 14, compared to HG as control. Blue dot indicates protein was significantly different at $p < 0.05$. (H) Gene ontology analysis of identified proteins from day 7 for biological processes (BP), molecular functions (MF), and cellular components (CC). (I) Gene ontology analysis of identified proteins from day 14 for BP, MF, and CC.

HG/MHAp, and HG/OGP/MHAp, respectively (Figure 6B,C). Cluster heatmap analysis indicated differences in protein expression patterns, forming two distinct clusters on day 7 and three clusters on day 14 (Figure 6D,E). Volcano plots demonstrated similar protein expression trends among groups on day 7, with HG/OGP/MHAp exhibiting a higher number of significantly expressed proteins compared to HG/OGP and HG/MHAp (Figure 6F). On day 14, HG/OGP showed a lower number of significant proteins than other groups, while HG/OGP/MHAp displayed fewer significant proteins compared to HG/MHAp (Figure 6G). Gene ontology (GO) enrichment analysis for biological processes (BP), molecular functions (MF), and cellular components (CC) revealed consistent trends between days 7 and 14 (Figure 6H,I). These results indicate that the incorporation of OGP and/or MHAp into the hydrogel induces distinct proteomics signatures in cPDLSCs potentially contributing to their osteogenic differentiation capacity.

The osteogenic potential of HG/OGP/MHAp on cPDLSCs is regulated by TGF-β, BMP, and Notch signaling pathways

To elucidate the molecular mechanisms underlying hydrogel-induced osteogenesis, signaling pathways regulating the osteogenic differentiation of cPDLSCs were analyzed using Reactome database (Figure 7A). The enrichment results identified several pathways potentially involved in osteogenic regulation, which are visualized in heatmap analysis (Figure 7B). Based on their relevance to bone formation, the Wnt, transforming growth factor-beta (TGF-β), bone morphogenic protein (BMP), and Notch signaling pathways were selected for further validation using specific inhibitors. As outlined in the experimental scheme (Figure 7C), cPDLSCs were treated with Dkk-1 (Wnt inhibitor), SB-431542 (TGF-β inhibitor), Dorsomorphin (BMP inhibitor), and DAPT (Notch inhibitor), and biomineralization was assessed on days 7 and 14. The result revealed that SB-431542, Dorsomorphin, and DAPT significantly reduced biomineralization at both time points, indicating the involvement of TGF-β, BMP, and Notch signaling in mediating osteogenesis (Figure 7D,E). In contrast, Dkk-1 treatment did not significantly affect mineral deposition. Collectively, these findings suggest that TGF-β, BMP, and Notch signaling pathways are critical regulators of the osteogenic differentiation of cPDLSCs induced by HG/OGP/MHAp.

Discussion

Injectable hydrogels represent a promising strategy for bone regeneration due to their excellent biocompatibility, minimally invasive delivery, and capability to incorporate both organic and inorganic bioactive agents. In this study, we developed an injectable SF-based hydrogel incorporating OGP and MHAp and evaluated its potential for promoting alveolar bone regeneration using cPDLSCs *in vitro*.

Characterization of the synthesized MHAp confirmed its nanoscale crystallinity and successful iron doping. The material was synthesized via a coprecipitation wet chemical method, and XRD analysis confirmed that the crystal structure of hydroxyapatite was preserved post-doping, consistent with previous findings (Wu et al. 2007). According to the definitions provided by the American Society for Testing and Materials (ASTM E2456–06, reapproved 2020) and ISO 80004-1:2023(E), nanoparticles are defined as particles with dimensions ranging from 1 to 100 nm. The synthesized MHAp met this criterion, as supported by both XRD and NTA, which confirmed that the majority of particles were within the nanoscale range. Morphological assessment by FE-SEM revealed spherical nanoparticles, in agreement with prior studies (Wu et al. 2007). Furthermore, FTIR analysis exhibited characteristic peaks corresponding to phosphate (v3 PO_4^{3-}), carbonate (v3 CO_3^{2-}), and hydroxyl (OH^-) groups in the ranges of 961–1091, 1400–1600, and 3200–3550 cm^{-1}, respectively, consistent with standard hydroxyapatite profiles (Koutsopoulos 2002; Varma and Babu 2005). The observed overlap of Fe–OH functional groups with the phosphate peak is indicative of successful Fe incorporation, as previously described (Mondal et al. 2017). Vibrating sample magnetometer (VSM) revealed a small hysteresis loop, confirming the superparamagnetic behavior of the Fe-doped HAp. Although the overall magnetization was low, it remained consistent with earlier studies utilizing a similar synthesis method (Wu et al. 2007), supporting its potential utility in magnetic-responsive biomedical applications.

Following the criteria established by the International Society for Cellular Therapy (ISCT), the isolated cPDLSCs used in this study were confirmed to exhibit MSC characteristics. These included plastic adherence,

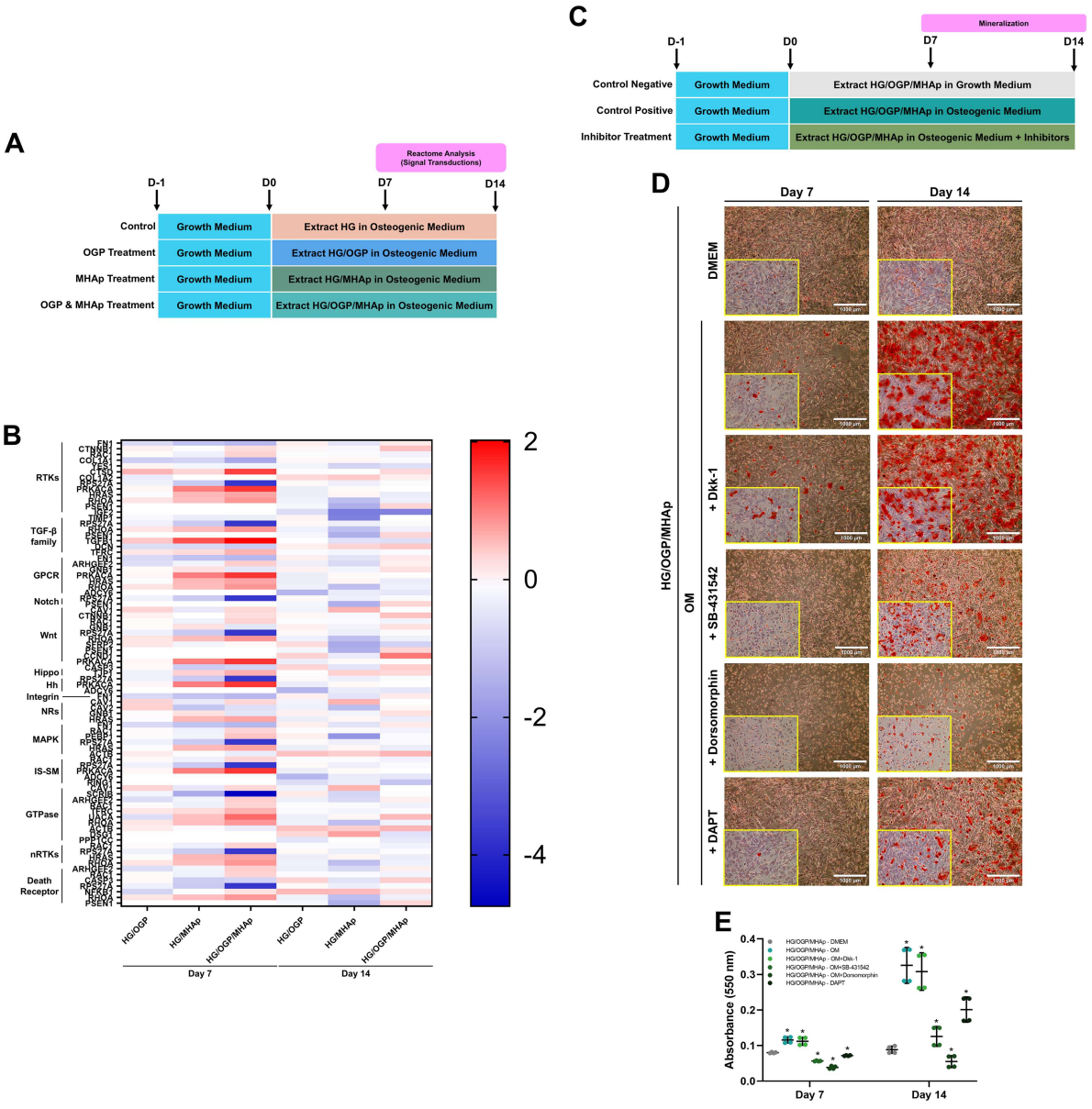

Figure 7. Functional validation of cPDLSCs under hydrogel treatment toward osteogenic lineage. (A) Experimental design. Identified proteins from days 7 and 14 were used for Reactome analysis. (B) Heatmap analysis of signaling pathway-related identified proteins compared to HG as control. (C) Experimental design. Inhibitors of relevant signaling pathways were used for functional validation of cPDLSCs under HG/OGP/MHAp for biomineralization staining. (D) Biomineralization staining of cPDLSCs under HG/OGP/MHAp treatment with and without relevant inhibitors by Alizarin Red S staining (representative image from four replicates). (E) Quantification of (D) by elution method ($n = 4$). * indicates the statistically significant difference to the control each day at $p < 0.05$, Mann–Whitney test; line indicates mean and standard deviation.

expression of defined MSC surface markers, and the ability for multilineage differentiation (Dominici et al. 2006). Additionally, the cells expressed key pluripotency and proliferation markers, further supporting their stemness profile (Nantavisai et al. 2020; Rodprasert et al. 2021; Dang Le et al. 2022; Taephatthanasagon et al. 2024). The presence of *S100A4* and *POSTN*, both of which are associated with periodontal ligament tissue, confirmed the origin of isolated cells (Iwata et al. 2009; Chen et al. 2013; Sedigh et al. 2023). Moreover, the colony-forming ability of cPDLSCs demonstrated their self-renewal and proliferative potential, which are essential properties of functional MSCs (Aponte and Caicedo 2017).

This study demonstrated that OGP promotes proliferation and exhibits no cytotoxic effects on cPDLSCs. The resazurin assay revealed a significant increase in metabolic activity, indicative of enhanced cell proliferation (Aslantürk 2018), and this finding was corroborated by L/D staining, which showed a greater number of viable, green-stained cells in the OGP-treated group. These results suggest that OGP possesses mitogenic activity toward cPDLSCs. Similar proliferative effects of OGP have been reported in various cell types, including human periodontal ligament stem cells (hPDLSCs), bone marrow-derived mesenchymal stem cells (BM-MSCs) of murine, rabbit, and human origin, osteoblastic MC3T3-E1 cells, osteogenic ROS 17/2.8 cells, and fibroblastic NIH 3T3 cells (Bab et al. 1992; Greenberg et al. 1993; Robinson et al. 1995; Fei et al. 2010; Purbantoro et al. 2022). Mechanistically, OGP is known to activate mitogen-activated protein kinase (MAPK) pathways via G_i protein-coupled receptors (GPCRs), thereby regulating cell proliferation (Gabarin et al. 2001). The CDK2/cyclin A axis has also been implicated in OGP-mediated cell cycle progression and proliferation enhancement (Fei et al. 2010).

This study demonstrated that MHAp exhibits the proliferation of cPDLSCs without inducing cytotoxic effects *in vitro*. Consistent with our findings, previous studies reported no significant cytotoxic differences between MHAp-treated and control groups on day 1 (Wu et al. 2007). Although a transient decline in proliferation was observed on day 5, this may reflect a lag phase in cellular growth rather than a toxic effect. By day 7, MHAp treatment led to a notable increase in cell proliferation, consistent with prior evidence showing that MHAp enhances the proliferation of MC3T3-E1 osteoblastic cells (He et al. 2017). The intrinsic magnetic properties of MHAp-containing scaffolds are known to influence cellular behavior by modulating ion channels and intracellular signaling, particularly after cellular internalization (Singh et al. 2014; Hu et al. 2018). The MHAp has also been known to activate the MAPK signaling pathway, a key regulator of cell proliferation (Zhang and Liu 2002; Wang et al. 2016). These findings suggested that MAPK activation may play a central role in the proliferative response of cPDLSCs to MHAp and possibly act synergistically with OGP to enhance cellular expansion.

The brownish appearance observed in HG/MHAp and HG/OGP/MHAp hydrogels was anticipated, as it reflects the intrinsic color of the synthesized MHAp. All hydrogels exhibited interconnected porous structures, consistent with previous reports on SF, sodium alginate (SA), and $CaCl_2$ composite hydrogels (Chuysinuan et al. 2021). The pore size observed in this study falls within the microporous range from 1 to 100 µm (Mays 2007), which is considered favorable for facilitating oxygen and nutrient delivery, vascularization, and bone ingrowth (Kattimani et al. 2016; Mukasheva et al. 2024). Notably, incorporation of OGP and/or MHAp led to a reduction in pore size, which may be attributed to increased cross-linking density and spatial occupation within the hydrogel matrix (Jing et al. 2019; Chuysinuan et al. 2021). FTIR spectroscopy further confirmed the chemical composition of the hydrogels. Characteristic peaks corresponding to amide I (1600–1700 cm^{-1}), amide II (1510–1530 cm^{-1}), and amide III (~1230 cm^{-1}) were detected, indicating the presence of silk fibroin (Jones et al. 2009; Yang et al. 2009; Aliramaji et al. 2017). Additionally, the phosphate (PO_4^{3-}) peak at 1028 cm^{-1} confirmed the successful incorporation of MHAp, while also suggesting effective crosslinking with SA (Koutsopoulos 2002; Varma and Babu 2005), implying the successful crosslinking with SA and MHAp.

The degradation profile revealed that the unmodified HG was almost completely degraded by day 14, whereas hydrogels containing MHAp retained approximately 60% of their structure. This finding suggested that the degradation of the hydrogels occurs through both chemical hydrolysis and enzymatic digestion, as previously reported (Chuysinuan et al. 2021). The presence of MHAp is likely to contribute to structural stabilization by enhancing resistance to degradation. Although MHAp is also biodegradable, it undergoes degradation through liquid-phase dissolution and cell-mediated resorption (Lu et al. 2002). In the present study, only liquid dissolution may have occurred in the experimental system. Hydrolysis of the hydrogel matrix is primarily attributed to the water-soluble nature of SA, which is susceptible to disruption by negatively charged repulsion within the swollen polymer network. Enzymatic degradation of SF is facilitated by protease XIV, which cleaves the protein at specific amino acid residues, including tyrosine (Tyr), phenylalanine (Phe), tryptophan (Trp), histidine (His), lysine (Lys), and arginine (Brown et al. 2015; Guo et al. 2020). As expected, the swelling profile exhibited an inverse trend to degradation: hydrogels with MHAp showed reduced swelling capacity. This reduction is likely due to MHAp altering the hydrogel architecture

by forming additional hydrogel bonds within the polymer network, thus decreasing water absorption. Additionally, the observed smaller pore size in MHAp-containing hydrogels may contribute to the reduced swelling capacity (Di Stefano et al. 2025). These trends are consistent with previous findings (Wu et al. 2020; Chuysinuan et al. 2021; Di Stefano et al. 2025). Mechanical testing revealed that the incorporation of OGP and/or MHAp decreased both compressive strength and stiffness. This reduction in mechanical performance is likely due to the disruption of the polymer network and limited interactions between organic and inorganic components, as similarly observed in previous work (Kim et al. 2017; Chuysinuan et al. 2021). Despite this, proliferation assays and L/D staining confirmed the cytocompatibility of all hydrogels with cPDLSCs in agreement with prior reports (Chuysinuan et al. 2021).

The observed enhancement of osteogenic differentiation in cPDLSCs following treatment with OGP- and/or MHAp-incorporated hydrogels highlights the therapeutic potential of this system for clinical bone regeneration applications. The OGP has been shown to stimulate osteogenic differentiation through multiple molecular mechanisms and signaling pathways, including RhoA/Rho-associated protein kinase, heme oxygenase-1 (HO-1), long non-coding RNA (lncRNA) AK141205, CXCL13, as well as canonical pathways, such as TGF-β, BMP, Wnt, Hedgehog, and Notch (Vanella et al. 2010; Chen et al. 2011; Li et al. 2015; Purbantoro et al. 2022). Similarly, MHAp has been reported to activate osteoinductive signaling cascades–including TGF-β, BMP, Wnt, Hedgehog, and Notch pathways–often following MAPK pathway stimulation (Brown et al. 1999; Riobo et al. 2006; Sapkota et al. 2007; Bikkavilli et al. 2008; Yamashita et al. 2013). In addition, MHAp has superior bone regenerative properties compared to the pristine nanohydroxyapatite (Hu et al. 2018; Russo et al. 2018). Interestingly, SF itself has been implicated in promoting osteogenesis through modulating Notch, Wnt, BMP, TGF-β, insulin-like growth factor (IGF), and platelet-derived growth factor (PDGF) pathways, further contributing to the differentiation process (Farokhi et al. 2018). Based on this collective evidence, it is reasonable to conclude that the enhanced osteogenic differentiation observed in this study results from a synergistic interaction among SF, OGP, and MHAp, rather than from any single component alone.

Given the demonstrated potential of the hydrogels for bone regeneration, a quantitative proteomics approach was performed to further investigate the phenomenon underlying the enhanced osteogenic differentiation of cPDLSCs *in vitro*. Comparative study with the control HG group revealed that incorporation of OGP and/or MHAp led to the regulation of unique proteome patterns, as illustrated by Venn diagrams and hierarchical cluster heat maps. Notably, a greater number of differentially expressed proteins were detected on day 7 compared to day 14. This decline in protein count over time may be attributed to the progression of cPDLSCs into the late stages of osteogenic differentiation, during which some cells underwent apoptosis, thereby reducing the viable cell population and detectable proteome complexity (Infante and Rodríguez 2018). These protein expression patterns were consistent with volcano plot analysis, which showed that HG/OGP-treated cells expressed fewer significantly regulated proteins compared to the HG/MHAp and HG/OGP/MHAp groups at both time points. Despite differences in the number and identity of proteins, GO analysis of BP, MF, and CC indicated similar trends across all groups. This suggests that while the treatments induced distinct proteomic profiles, the underlying biological dynamics governing osteogenic differentiation were largely conserved. These findings emphasize that each hydrogel composition modulates a unique proteomic landscape while contributing to a shared osteogenic trajectory.

To further elucidate the molecular mechanisms driving the osteogenic differentiation of cPDLSCs under hydrogel treatment, Reactome pathway enrichment analysis was conducted. This analysis revealed activation of key osteogenic-related signaling pathways, including TGF-β superfamily, Wnt, and Notch pathways, which are known to play main roles in MSC differentiation toward the osteogenic lineage (Deng et al. 2008; Chen et al. 2016). To validate the functional relevance of these pathways, selective inhibitors were employed: SB-431542 for TGF-β, Dorsomorphin for BMP, DAPT for Notch, and Dkk-1 for canonical Wnt signaling. Significant reductions in biomineralization following treatment with SB-431542, Dorsomorphin, and DAPT confirm that TGF-β, BMP, and Notch signaling pathways are critical mediators of osteogenesis induced by HG/OGP/MHAp. The TGF-β and BMP belong to the same signaling family and are well-established regulators of bone formation (Wang et al. 2025). This study also observed dynamic regulation of TGFB1, which was upregulated on day 7 and downregulated on day 14, suggesting a time-dependent

activation of TGF-β signaling that could be effectively attenuated through pathway inhibition. Notably, DAPT significantly suppressed biomineralization, supporting the role of Notch signaling in early osteogenic commitment, as previously reported (Purbantoro et al. 2022). Additionally, BMP signaling has been shown to interact with and influence Notch activation during osteogenesis (Manokawinchoke et al. 2021), further supporting their independent regulatory roles. There was no significant difference in biomineralization between cPDLSCs treated with or without Dkk-1, suggesting that canonical Wnt signaling may not play a dominant role in osteogenic differentiation under HG/OGP/MHAp treatment. This contrasts with previous findings where Dkk-1 inhibited biomineralization in human PDLSCs under interleukin-6 (IL-6) stimulation (Purwaningrum et al. 2023). The Dkk-1 is a well-established inhibitor of the canonical Wnt pathway and functions by binding to the LRP5/6 co-receptors, thereby blocking Wnt ligand signaling (Liu et al. 2022). This pro-osteogenic effect of Dkk-1 found in this study is assumed to be caused by the osteogenic differentiation of cPDLSCs is either Wnt-independent or Wnt-non-canonical-dependent. Similar findings have been reported in canine dental pulp stem cells (cDPSCs), where Dkk-1 promoted rather than suppressed osteogenic differentiation (Nantavisai et al. 2020). Mechanistically, Dkk-1 has been shown to upregulate *Runx2* expression under specific conditions, which can lead to enhanced osteogenesis (Liu et al. 2022). These context-dependent effects highlight the complexity of Wnt signaling, which can vary across cell types and experimental conditions (Grotheer et al. 2021). Therefore, the influence of Dkk-1 may be modulated by cell-intrinsic factors or by crosstalk with other signaling pathways in the differentiation microenvironment.

In conclusion, the injectable SF hydrogel incorporating OGP and MHAp exhibited non-cytotoxic, demonstrated excellent biocompatibility, promoted cPDLSCs proliferation, and significantly enhanced osteogenic differentiation *in vitro*. These effects were predominantly mediated through the activation of TGF-β, BMP, and Notch signaling pathways (Figure 8). Given its injectability, bioactivity, and safety profile, this hydrogel system holds strong potential for clinical translation, particularly for the treatment of alveolar bone defects in veterinary medicine.

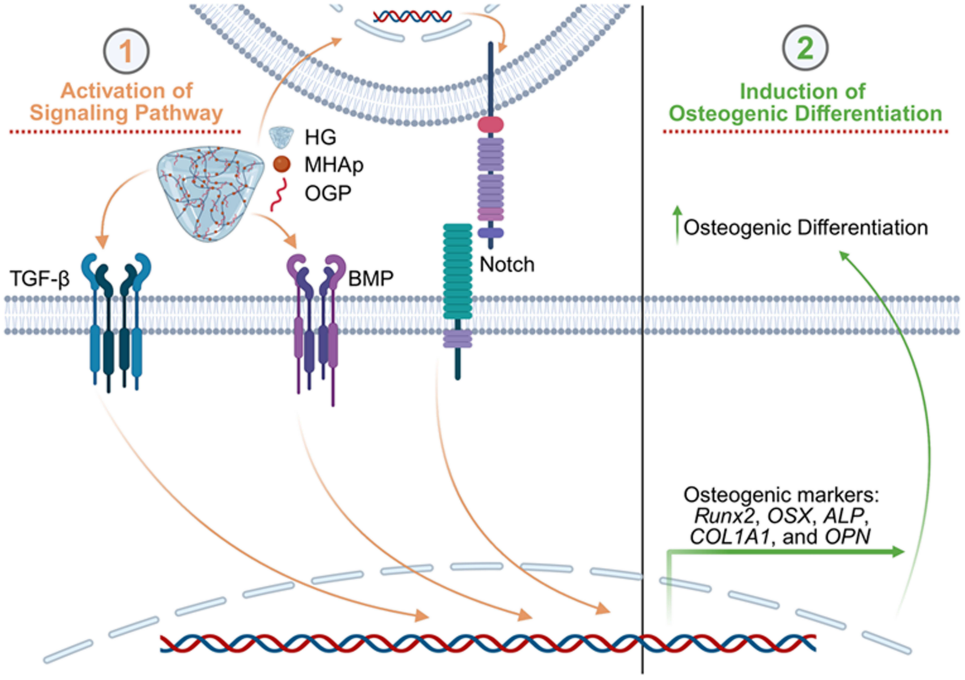

Figure 8. Summary of signaling pathways involved in osteogenic differentiation of cPDLSCs under hydrogel treatment. (1) HG/OGP/MHAp activates TGF-β, BMP, and Notch signaling pathways. (2) The activation leads to the expression of osteogenic markers that result in increased osteogenic differentiation of cPDLSCs. Note: HG = hydrogel, MHAp = magnetic nanohydroxyapatite, OGP = osteogenic growth peptide, TGF-β = transforming growth factor β, BMP = bone morphogenic protein, OSX = osterix, ALP = alkaline phosphatase, COL1A1 = collagen type I alpha 1 chain, OPN = osteopontin.

Acknowledgements

This work (Grant No. Research Grant for New Scholar (RGNS) 65-023) was supported by the Office of the Permanent Secretary, Ministry of Higher Education, Science, Research, and Innovation (OPS MHESI), Thailand Science Research and Innovation (TSRI) and Chulalongkorn University and the Research Grant, Faculty of Veterinary Science, Chulalongkorn University. S.D.P was supported by The Second Century Fund (C2F), Chulalongkorn University for Doctoral Scholarship, and the 90th Anniversary of Chulalongkorn University. C.S. was supported by the Research Supporting Grant, Faculty of Veterinary Science, Chulalongkorn University; the Ratchadaphiseksomphot Endowment Fund, Chulalongkorn University; the Veterinary Clinical Stem Cell and Bioengineering Research Unit, Chulalongkorn University; and the Thailand Science Research and Innovation Fund, Chulalongkorn University. The authors would like to acknowledge Dr. Kitti Torrungruang for his assistance in facilitating laboratory support and the Small Animal Teaching Hospital, Faculty of Veterinary Science, Chulalongkorn University for supporting the collection of periodontal ligament tissue samples used in this study.

Disclosure statement

No potential conflict of interest was reported by the author(s).

Data availability statement

The accession number for the proteomics data deposited to the ProteomeXchange Consortium via the PRoteomics IDEntifications (PRIDE) partner repository is PXD063171.

Author contributions

CRediT: **Steven Dwi Purbantoro:** Conceptualization, Investigation, Methodology, Writing – original draft; **Marta Scatena:** Methodology, Supervision, Writing – review & editing; **Teeanutree Taephatthanasagon:** Methodology; **Watchareewan Rodprasert:** Methodology; **Poorichaya Somparn:** Methodology, Supervision; **Saharat Nanthawong:** Methodology; **Jiradej Makjaroen:** Methodology, Supervision; **Pongsakorn Jantaratana:** Methodology; **Rangsini Mahanonda:** Methodology; **Noppadol Sa-Ard-Iam:** Methodology; **Thanaphum Osathanon:** Supervision, Writing – review & editing; **Sirinun Pisamai Tabtieang:** Supervision; **Chenphop Sawangmake:** Conceptualization, Supervision, Writing – review & editing; **Sirirat Rattanapuchpong:** Conceptualization, Methodology, Supervision, Writing – review & editing.

References

Aliramaji S, Zamanian A, Mozafari M. 2017. Super-paramagnetic responsive silk fibroin/chitosan/magnetite scaffolds with tunable pore structures for bone tissue engineering applications. Mater Sci Eng C. 70:736–744. https://doi.org/10.1016/j.msec.2016.09.039

Aponte PM, Caicedo A. 2017. Stemness in cancer: stem cells, cancer stem cells, and their microenvironment. Stem Cells Int. 2017(1):5619472.

Aslantürk ÖS. 2018. In vitro cytotoxicity and cell viability assays: principles, advantages, and disadvantages. In: Larramendy Marcelo L., Soloneski Sonia, editors. Genotoxicity—a predictable risk to our actual world. IntechOpen. p 64–80. https://doi.org/10.5772/intechopen.71923

Bab I et al. 1992. Histone H4-related osteogenic growth peptide (OGP): a novel circulating stimulator of osteoblastic activity. EMBO J. 11(5):1867–1873. https://doi.org/10.1002/j.1460-2075.1992.tb05238.x

Bikkavilli RK, Feigin ME, Malbon CC. 2008. p38 mitogen-activated protein kinase regulates canonical Wnt–β-catenin signaling by inactivation of GSK3β. J Cell Sci. 121(21):3598–3607. https://doi.org/10.1242/jcs.032854

Brown J, Lu C-L, Coburn J, Kaplan DL. 2015. Impact of silk biomaterial structure on proteolysis. Acta Biomater. 11:212–221. https://doi.org/10.1016/j.actbio.2014.09.013

Brown JD, DiChiara MR, Anderson KR, Gimbrone MA, Topper JN. 1999. MEKK-1, a component of the stress (stress-activated protein kinase/c-Jun N-terminal kinase) pathway, can selectively activate Smad2-mediated transcriptional activation in endothelial cells. J Biol Chem. 274(13):8797–8805. https://doi.org/10.1074/jbc.274.13.8797

Chen K, Xiong H, Huang Y, Liu C. 2013. Comparative analysis of in vitro periodontal characteristics of stem cells from apical papilla (SCAP) and periodontal ligament stem cells (PDLSCs). Arch Oral Biol. 58(8):997–1006. https://doi.org/10.1016/j.archoralbio.2013.02.010

Chen Q et al. 2016. Fate decision of mesenchymal stem cells: adipocytes or osteoblasts? Cell Death Differ. 23(7):1128–1139.

Chen Z et al. 2011. Synthetic osteogenic growth peptide promotes differentiation of human bone marrow mesenchymal stem cells to osteoblasts via RhoA/ROCK pathway. Mol Cell Biochem. 358(1):221–227. https://doi.org/10.1007/s11010-011-0938-7

Chon J-W et al. 2012. Silk fibroin hydrolysate inhibits osteoclastogenesis and induces apoptosis of osteoclasts derived from RAW 264.7 cells. Int J Mol Med. 30(5):1203–1210. https://doi.org/10.3892/ijmm.2012.1120
Chuysinuan P et al. 2021. Injectable eggshell-derived hydroxyapatite-incorporated fibroin-alginate composite hydrogel for bone tissue engineering. Int J Biol Macromol. 193:799–808. https://doi.org/10.1016/j.ijbiomac.2021.10.132
Ciocci M, Cacciotti I, Seliktar D, Melino S. 2018. Injectable silk fibroin hydrogels functionalized with microspheres as adult stem cells-carrier systems. Int J Biol Macromol. 108:960–971. https://doi.org/10.1016/j.ijbiomac.2017.11.013
Colombo A et al. 2017. Clinical and microbiological parameters of naturally occurring periodontitis in the non-human primate Macaca mulatta. J Oral Microbiol. 9(1):1403843. https://doi.org/10.1080/20002297.2017.1403843
Dang Le Q et al. 2022. In vitro generation of transplantable insulin-producing cells from canine adipose-derived mesenchymal stem cells. Sci Rep. 12(1):1–18. https://doi.org/10.1038/s41598-022-13114-3
Deng Z-L et al. 2008. Regulation of osteogenic differentiation during skeletal development. Front Biosci. 13(1):2001–2021.
Di Stefano A et al. 2025. Effect of nanocomposite chitosan/hydroxyapatite pH-induced hydrogels on the osteogenic differentiation of spheroids from adipose stem cells. Int J Biol Macromol. 299:140213. https://doi.org/10.1016/j.ijbiomac.2025.140213
Dominici M et al. 2006. Minimal criteria for defining multipotent mesenchymal stromal cells. The International Society for Cellular Therapy position statement. Cytotherapy. 8(4):315–317. https://doi.org/10.1080/14653240600855905
Farokhi M et al. 2018. Silk fibroin/hydroxyapatite composites for bone tissue engineering. Biotech Adv. 36(1):68–91. https://doi.org/10.1016/j.biotechadv.2017.10.001
Fei Q et al. 2010. Osteogenic growth peptide enhances the proliferation of bone marrow mesenchymal stem cells from osteoprotegerin-deficient mice by CDK2/cyclin A. Acta Biochim Biophys Sin. 42(11):801–806. https://doi.org/10.1093/abbs/gmq086
Gabarin N et al. 2001. Mitogenic Gi protein-MAP kinase signaling cascade in MC3T3-E1 osteogenic cells: activation by C-terminal pentapeptide of osteogenic growth peptide [OGP (10–14)] and attenuation of activation by cAMP. J Cell Biochem. 81(4):594–603. https://doi.org/10.1002/jcb.1083
Gioso M, Shofer F, Barros P, Harvey C. 2001. Mandible and mandibular first molar tooth measurements in dogs: relationship of radiographic height to body weight. J Vet Dent. 18(2):65–68. https://doi.org/10.1177/089875640101800202
Greenberg Z et al. 1993. Mitogenic action of osteogenic growth peptide (OGP) role of amino and carboxy-terminal regions and charge. Biochim Biophys Acta Mol Cell Res. 1178(3):273–280. https://doi.org/10.1016/0167-4889(93)90204-3
Grotheer V, Skrynecki N, Oezel L, Windolf J, Grassmann J. 2021. Osteogenic differentiation of human mesenchymal stromal cells and fibroblasts differs depending on tissue origin and replicative senescence. Sci Rep. 11(1):11968. https://doi.org/10.1038/s41598-021-91501-y
Guo C, Li C, Kaplan DL. 2020. Enzymatic degradation of Bombyx mori silk materials: a review. Biomacromolecules. 21(5):1678–1686. https://doi.org/10.1021/acs.biomac.0c00090
He J et al. 2017. A magnetic hydroxyapatite composite scaffold-based magnetic therapy for bone repair: an experimental study in canis lupus familiaris. Regen Biomater. 4(2):97–103. https://doi.org/10.1093/rb/rbw039
Hienz SA, Paliwal S, Ivanovski S. 2015. Mechanisms of bone resorption in periodontitis. J Immunol Res. 2015(1):615486.
Hitti RA, Kerns DG. 2011. Guided bone regeneration in the oral cavity: a review. Open Pathol J. 5(1):33–45. https://doi.org/10.2174/1874375701105010033
Hu S et al. 2018. Enhanced bone regeneration and visual monitoring via superparamagnetic iron oxide nanoparticle scaffold in rats. J Tissue Eng Regen Med. 12(4):e2085–e2098. https://doi.org/10.1002/term.2641
Infante A, Rodríguez CI. 2018. Osteogenesis and aging: lessons from mesenchymal stem cells. Stem Cell Res Ther. 9(1):1–7. https://doi.org/10.1186/s13287-018-0995-x
Iwata T et al. 2009. Periodontal regeneration with multi-layered periodontal ligament-derived cell sheets in a canine model. Biomaterials. 30(14):2716–2723. https://doi.org/10.1016/j.biomaterials.2009.01.032
Jing J, Liang S, Yan Y, Tian X, Li X. 2019. Fabrication of hybrid hydrogels from silk fibroin and tannic acid with enhanced gelation and antibacterial activities. ACS Biomater Sci Eng. 5(9):4601–4611. https://doi.org/10.1021/acsbiomaterials.9b00604
Jones GL, Motta A, Marshall MJ, El Haj AJ, Cartmell SH. 2009. Osteoblast: osteoclast co-cultures on silk fibroin, chitosan and PLLA films. Biomaterials. 30(29):5376–5384. https://doi.org/10.1016/j.biomaterials.2009.07.028
Junka AF et al. 2015. Microbial biofilms are able to destroy hydroxyapatite in the absence of host immunity in vitro. J Oral Maxillof Surg. 73(3):451–464. https://doi.org/10.1016/j.joms.2014.09.019
Kattimani VS, Kondaka S, Lingamaneni KP. 2016. Hydroxyapatite–-past, present, and future in bone regeneration. Bone Tissue Regen Insights. 7:BTRI.S36138. https://doi.org/10.4137/BTRI.S36138. BTRI. S36138.
Kim MH et al. 2017. Silk fibroin/hydroxyapatite composite hydrogel induced by gamma-ray irradiation for bone tissue engineering. Biomater Res. 21(1):1–9. https://doi.org/10.1186/s40824-017-0098-2
Könönen E, Gursoy M, Gursoy UK. 2019. Periodontitis: a multifaceted disease of tooth-supporting tissues. J Clin Med. 8(8):1135. https://doi.org/10.3390/jcm8081135
Koutsopoulos S. 2002. Synthesis and characterization of hydroxyapatite crystals: a review study on the analytical methods. J Biomed Mater Res. 62(4):600–612. https://doi.org/10.1002/jbm.10280

Kurt-Bayrakdar S et al. 2024. Detection of periodontal bone loss patterns and furcation defects from panoramic radiographs using deep learning algorithm: a retrospective study. BMC Oral Health. 24(1):155.
Li H, Zhang Z, Chen Z, Zhang D. 2015. Osteogenic growth peptide promotes osteogenic differentiation of mesenchymal stem cells mediated by LncRNA AK141205-induced upregulation of CXCL13. Biochem Biophys Res Commun. 466(1):82–88. https://doi.org/10.1016/j.bbrc.2015.08.112
Li X et al. 2019. Severe periodontitis may influence cementum and dental pulp through inflammation, oxidative stress, and apoptosis. J Periodontol. 90(11):1297–1306. https://doi.org/10.1002/JPER.18-0604
Liu J et al. 2022. Wnt/β-catenin signalling: function, biological mechanisms, and therapeutic opportunities. Signal Transduct Target Ther. 7(1):3. https://doi.org/10.1038/s41392-021-00762-6
Lu J et al. 2002. The biodegradation mechanism of calcium phosphate biomaterials in bone. J Biomed Mater Res. 63(4):408–412. https://doi.org/10.1002/jbm.10259
Ma Y, Yang J, Hu Y, Xia Z, Cai K. 2022. Osteogenic differentiation of the MSCs on silk fibroin hydrogel loaded Fe3O4@ PAA NPs in static magnetic field environment. Colloids Surf, B. 220:112947. https://doi.org/10.1016/j.colsurfb.2022.112947
Manokawinchoke J, Watcharawipas T, Ekmetipunth K, Jiamjirachart M, Osathanon T. 2021. Dorsomorphin attenuates Jagged1-induced mineralization in human dental pulp cells. Int Endod J. 54(12):2229–2242. https://doi.org/10.1111/iej.13620
Mays T. 2007. A new classification of pore sizes. In: Llewellyn P. L., Rodriquez-Reinoso F., Rouqerol J., Seaton N., editors. Studies in surface science and catalysis. Vol. 160. Elsevier. p 57–62. https://doi.org/10.1016/S0167-2991(07)80009-7
Mondal S et al. 2017. Magnetic hydroxyapatite: a promising multifunctional platform for nanomedicine application. Int J Nanomedicine. 12:8389–8410. https://doi.org/10.2147/IJN.S147355
Mukasheva F et al. 2024. Optimizing scaffold pore size for tissue engineering: insights across various tissue types. Front Bioeng Biotechnol. 12:1444986. https://doi.org/10.3389/fbioe.2024.1444986
Nantavisai S et al. 2020. Systems biology analysis of osteogenic differentiation behavior by canine mesenchymal stem cells derived from bone marrow and dental pulp. Sci Rep. 10(1):1–18. https://doi.org/10.1038/s41598-020-77656-0
Niemiec BA. 2008. Periodontal disease. Top Companion Anim Med. 23(2):72–80. https://doi.org/10.1053/j.tcam.2008.02.003
Purbantoro SD, Osathanon T, Nantavisai S, Sawangmake C. 2022. Osteogenic growth peptide enhances osteogenic differentiation of human periodontal ligament stem cells. Heliyon. 8(7):e09936. https://doi.org/10.1016/j.heliyon.2022.e09936
Purwaningrum M, Giachelli CM, Osathanon T, Rattanapuchpong S, Sawangmake C. 2023. Dissecting specific Wnt components governing osteogenic differentiation potential by human periodontal ligament stem cells through interleukin-6. Sci Rep. 13(1):9055. https://doi.org/10.1038/s41598-023-35569-8
Riobo NA, Haines GM, Emerson JC. 2006. Protein kinase C-δ and mitogen-activated protein/extracellular signal–regulated kinase-1 control GLI activation in Hedgehog signaling. CaRes. 66(2):839–845. https://doi.org/10.1158/0008-5472.CAN-05-2539
Robinson D, Bab I, Nevo Z. 1995. Osteogenic growth peptide regulates proliferation and osteogenic maturation of human and rabbit bone marrow stromal cells. J Bone Miner Res. 10(5):690–696. https://doi.org/10.1002/jbmr.5650100504
Rodprasert W et al. 2021. Tailored generation of insulin producing cells from canine mesenchymal stem cells derived from bone marrow and adipose tissue. Sci Rep. 11(1):1–17. https://doi.org/10.1038/s41598-021-91774-3
Russo A et al. 2018. Bone regeneration in a rabbit critical femoral defect by means of magnetic hydroxyapatite macroporous scaffolds. J Biomed Mater Res B Appl Biomater. 106(2):546–554. https://doi.org/10.1002/jbm.b.33836
Sapkota G, Alarcón C, Spagnoli FM, Brivanlou AH, Massagué J. 2007. Balancing BMP signaling through integrated inputs into the Smad1 linker. Mol Cell. 25(3):441–454. https://doi.org/10.1016/j.molcel.2007.01.006
Sawangmake C, Nantavisai S, Osathanon T, Pavasant P. 2016. Osteogenic differentiation potential of canine bone marrow-derived mesenchymal stem cells under different β-glycerophosphate concentrations in vitro. Thai J Vet Med. 46(4):617–625. https://doi.org/10.56808/2985-1130.2781
Scherer E, Hetzel S, Snyder CJ. 2019. Assessment of the role of the mandibular first molar tooth in mandibular fracture patterns of 29 dogs. J Vet Dent. 36(1):32–39. https://doi.org/10.1177/0898756419846183
Sedigh HS et al. 2023. In vitro investigation of canine periodontal ligament-derived mesenchymal stem cells: a possibility of promising tool for periodontal regeneration. J Oral Biol Craniofac Res. 13(3):403–411. https://doi.org/10.1016/j.jobcr.2023.03.010
Singh RK et al. 2014. Potential of magnetic nanofiber scaffolds with mechanical and biological properties applicable for bone regeneration. PLoS One. 9(4):e91584. https://doi.org/10.1371/journal.pone.0091584
Sueishi T et al. 2020. GRK 5 inhibition attenuates cartilage degradation via decreased NF-κB signaling. Arthritis Rheumatol. 72(4):620–631.
Sun W, Gregory DA, Tomeh MA, Zhao X. 2021. Silk fibroin as a functional biomaterial for tissue engineering. Int J Mol Sci. 22(3):1499. https://doi.org/10.3390/ijms22031499
Taephatthanasagon T et al. 2024. Osteogenic potentials in canine mesenchymal stem cells: unraveling the efficacy of polycaprolactone/hydroxyapatite scaffolds in veterinary bone regeneration. BMC Vet Res. 20(1):403. https://doi.org/10.1186/s12917-024-04246-x
Tanasa E et al. 2020. Impact of the magnetic field on 3T3-E1 preosteoblasts inside SMART silk fibroin-based scaffolds decorated with magnetic nanoparticles. Mater Sci Eng C. 110:110714. https://doi.org/10.1016/j.msec.2020.110714

Torsahakul C et al. 2022. Bio-fabrication of stem-cell-incorporated corneal epithelial and stromal equivalents from silk fibroin and gelatin-based biomaterial for canine corneal regeneration. PLoS One. 17(2):e0263141. https://doi.org/10.1371/journal.pone.0263141

Vanella L et al. 2010. HO-1 expression increases mesenchymal stem cell-derived osteoblasts but decreases adipocyte lineage. Bone. 46(1):236–243. https://doi.org/10.1016/j.bone.2009.10.012

Varma H, Babu SS. 2005. Synthesis of calcium phosphate bioceramics by citrate gel pyrolysis method. Ceram Int. 31(1):109–114. https://doi.org/10.1016/j.ceramint.2004.03.041

Wang L, Ruan M, Bu Q, Zhao C. 2025. Signaling pathways driving MSC osteogenesis: mechanisms, regulation, and translational applications. Int J Mol Sci. 26(3):1311. https://doi.org/10.3390/ijms26031311

Wang Q et al. 2016. Response of MAPK pathway to iron oxide nanoparticles in vitro treatment promotes osteogenic differentiation of hBMSCs. Biomaterials. 86:11–20. https://doi.org/10.1016/j.biomaterials.2016.02.004

Wang Y et al. 2020. Silk fibroin/sodium alginate composite porous materials with controllable degradation. Int J Biol Macromol. 150:1314–1322. https://doi.org/10.1016/j.ijbiomac.2019.10.141

Wiebe CB, Adkins CA, Putnins EE, Hakkinen L, Larjava HS. 2001. Naturally occurring periodontal bone loss in the wild deer mouse, genus *Peromyscus*. J Periodontol. 72(5):620–625. https://doi.org/10.1902/jop.2001.72.5.620

Wu H-C, Wang T-W, Sun J-S, Wang W-H, Lin F-H. 2007. A novel biomagnetic nanoparticle based on hydroxyapatite. Nanot. 18(16):165601. https://doi.org/10.1088/0957-4484/18/16/165601

Wu J et al. 2020. Stem cell-laden injectable hydrogel microspheres for cancellous bone regeneration. Chem Eng J. 393:124715. https://doi.org/10.1016/j.cej.2020.124715

Yamashita AS et al. 2013. Notch pathway is activated by MAPK signaling and influences papillary thyroid cancer proliferation. Transl Oncol. 6(2):197–IN22. https://doi.org/10.1593/tlo.12442

Yang M-C et al. 2009. The cardiomyogenic differentiation of rat mesenchymal stem cells on silk fibroin–polysaccharide cardiac patches in vitro. Biomaterials. 30(22):3757–3765. https://doi.org/10.1016/j.biomaterials.2009.03.057

Zhang W, Liu HT. 2002. MAPK signal pathways in the regulation of cell proliferation in mammalian cells. Cell Res. 12(1):9–18. https://doi.org/10.1038/sj.cr.7290105

Zhu W, Liang M. 2015. Periodontal ligament stem cells: current status, concerns, and future prospects. Stem Cells Int. 2015:1–11. https://doi.org/10.1155/2015/972313